Science in China Series G: Physics, Mechanics & Astronomy

Springer

www.scichina.com
phys.scichina.com
www.springerlink.com

Limitations of absolute current densities derived from the Semel & Skumanich method

LI Jing[1†] & FAN YuHong[2]

[1] Institute for Astronomy, University of Hawaii, 2680 Woodlawn Drive, Honolulu, HI 96822, USA;

[2] High Altitude Observatory, Earth and Sun Systems Laboratory, National Center for Atmospheric Research, P.O. Box 3000, Boulder, CO 80307, USA

Semel and Skumanich proposed a method to obtain the absolute electric current density, $|J_z|$, without disambiguation of 180° in the transverse field directions. The advantage of the method is that the uncertainty in the determination of the ambiguity in the magnetic azimuth is removed. Here, we investigate the limits of the calculation when applied to a numerical MHD model. We have found that the combination of changes in the magnetic azimuth with vanishing horizontal field component leads to errors, where electric current densities are often strong. Where errors occur, the calculation gives $|J_z|$ too small by factors typically 1.2 – 2.0.

numerical MHD model, magnetic field, electric current density

The electric current density is an important measure of the non-potentiality of the magnetic field in solar active regions. It has the potential to illuminate the active region eruption process. Vertical electric current densities can be calculated from vector magnetic fields measured in the photosphere. They have been repeatedly obtained ever since photospheric vector magnetic fields first became routinely available in the 1980s[1−15]. All these calculations involve the resolution of the 180° ambiguity in the transverse field directions, which problem is caused by the diagnosis of the magnetic field via the Zeeman effect. Semel & Skumanich[16] developed a method to calculate the absolute vertical electric current density from observed vector magnetic fields. Their formulation is especially interesting in that it does not require the 180° disambiguation of the transverse field directions and therefore removes one uncertainty in the current calculation.

The Semel & Skumanich method can be outlined as follows. In SI units, Ampère's law reads $\mu_0 \boldsymbol{J} = \nabla \times \boldsymbol{B}$, where $\boldsymbol{J}$ is the current density and μ_0 is the permittivity of the vacuum. Since $\mu_0 = 4\pi \times 10^{-7}$ T·mA^{-1}, then $4\pi J_z = \frac{\partial B_y}{\partial x} - \frac{\partial B_x}{\partial y}$, where the magnetic field is measured in G and the current density is measured in mA m^{-2}, and the distances are measured in m. Multiplying both sides of the J_z equation by B_x^4, B_y^4, and $B_x B_y$, $B_y B_x$, we obtain an expression for $[(\nabla \times \boldsymbol{B})_z]^2 = B_x^2 g_y^2 + B_y^2 g_x^2 - B_\perp^2 g_x g_y \sin 2\phi$ which is equivalent to

$$|\nabla \times \boldsymbol{B}|_z = B_x g_y - B_y g_x. \quad (1)$$

Here, g_x, g_y are given by

Received October 2008; accepted June 2009
doi: 10.1007/s11433-009-0272-1

†Corresponding author (email: jingucla@gmail.com); Current Address: UCLA Institute of Geophysics and Planetary Physics, 2713 Geology Building, MG 951567 Los Angeles, CA 90095-1567, USA

Citation: Li J, Fan Y H. Limitations of absolute current densities derived from the Semel & Skumanich method. Sci China Ser G, 2009, 52(11): 1678-1685, doi: 10.1007/s11433-009-0272-1

$$B_\perp^4 g_x = B_y^2 \frac{\partial(B_x B_y)}{\partial y} - \frac{1}{2} B_x B_y \frac{\partial(B_y^2 - B_x^2)}{\partial y} - \frac{1}{2} B_\perp^2 \frac{\partial B_y^2}{\partial x}, \quad (2)$$

$$B_\perp^4 g_y = B_x^2 \frac{\partial(B_x B_y)}{\partial x} - \frac{1}{2} B_x B_y \frac{\partial(B_x^2 - B_y^2)}{\partial x} - \frac{1}{2} B_\perp^2 \frac{\partial B_x^2}{\partial y}, \quad (3)$$

where $B_\perp = \sqrt{B_x^2 + B_y^2}$, the strength of the horizontal magnetic component; $B_x = B_\perp \cos\phi$ and $B_y = B_\perp \sin\phi$ are two perpendicular horizontal components and ϕ is the magnetic azimuth. All are observable quantities, but $[(\nabla \times \boldsymbol{B})_z]^2$ does not vary with either ϕ or $\phi + 180°$.

Recently[17], we used eq. (1) to calculate the absolute vertical current densities in two morphologically different active regions: a simple sunspot region free of flare activity (NOAA 10001 on June 20, 2002); and an active region of the quadrupolar configuration with multiple flares (including a white light X3 flare[18]) and coronal mass ejections (NOAA 10030 on July 15, 2002). We found that $|J_z|$ correlated with vertical magnetic field, $B_\parallel$, in the form $|J_z| = a + b|B_\parallel|$ for both regions on large scales. The relationship between $|J_z|$ and $|B_\parallel|$ needs to be examined with more samples of active regions, and observational data from different instruments. Nevertheless, we realize that the use of $|J_z|$ has the potential to characterize active regions in their flare productivity. The absolute vertical current density is particularly useful for studying the mechanical forces due to currents induced in moving material[19].

Equation (1) is limited by the lack of disambiguation of the 180° in the magnetic azimuth. Semel & Skumanich[16] pointed out that the calculation "blindly" follows the magnetic field continuity, leading to failure when (1) the magnetic azimuth suddenly changes direction; (2) the horizontal component simply vanishes paralyzing the continuous magnetic field assumption. In this short paper, we explore the limits of the $|J_z|$ calculation with reference to a MHD numerical simulation developed by Fan & Gibson[20,21].

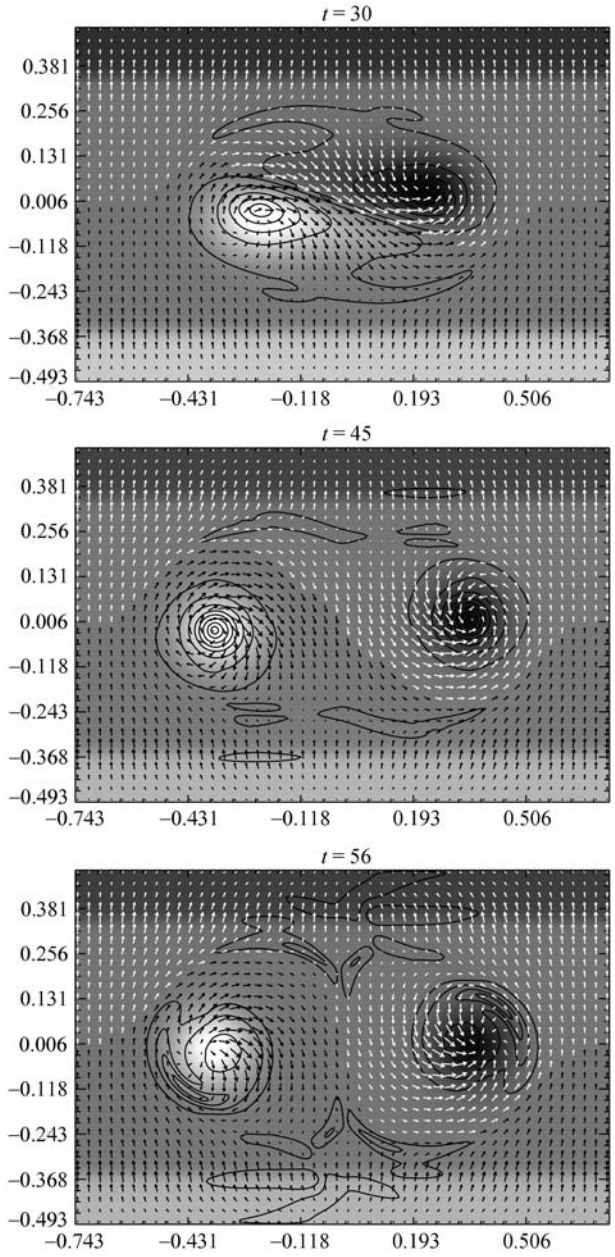

Figure 1 The MHD simulations at $t = 30, 45, 56$ in the xy-plane above the lower boundary, $z = 0.00625L$. The background images are the vertical magnetic field, B_z. The horizontal magnetic fields are plotted in arrows: white arrows correspond to $B_z < 0$, and black arrows correspond to $B_z \geqslant 0$. Directions of arrows represent $\boldsymbol{B}_\perp$ directions, and the lengths of the arrows represent $\boldsymbol{B}_\perp$ strengths. The absolute vertical current densities, $|J_z|$, are plotted in contours, $|J_z| = 0.01, 0.04, 0.08, 0.12, 0.15, 0.18, 0.21, 0.23$.

1 MHD model

A 3-dimensional numerical simulation of the coronal response to a rising flux tube was presented by

Fan & Gibson[20,21]. The system reaches instability when the flux tube contains a twist of $1.875 \times 2\pi$ turns about the tube axis between two footpoints. In this work, we use the simulation at three times corresponding to different phases of the flux tube evolution. At $t = 30$ (all times are given in arbitrary units), the flux tube axis rises above the lower boundary at a sub-Alfvénic speed. At $t = 45$, the flux tube contains $1.5 \times 2\pi$ turns between the footpoints above the lower boundary. The tube undergoes a significant acceleration with both writhing and rising motions, but it stays in a 2-dimensional plane. At $t = 56$, the flux tube contains $1.875 \times 2\pi$ twists between the two footpoints. The simulation reaches the critical point at the onset of the kink instability. The complexity of the model is represented by the turns of the flux tube, which grows with increasing time.

The model is built in a Cartesian domain in a box with resolution, $240 \times 160 \times 200$ in the units $x = [-0.75L, 0.75L], y = [-0.5L, 0.5L], z = [0, 1.25L]$, where L is the length of the box edges. In our work, the "photospheric magnetic field" is the field at $z = 0.003125L$ just above the lower boundary. Figure 1 shows the 2-dimensional magnetic fields in the model at the three times. The vertical magnetic fields, B_z, are the background images. The horizontal fields, $\boldsymbol{B}_\perp$, are plotted with short arrow bars: white arrow bars correspond to $B_z < 0$, and black ones correspond to $B_z \geqslant 0$. $|J_z|$ are plotted as contours over the magnetic fields.

2 Errors in the $|J_z|$ calculation

Errors from the application of eq. (1) are evaluated by comparing the true ($|J_z|$) with the derived current density ($|J_z|_{ss}$) after excluding the current density on the edges of the simulation box (it is apparent that the current densities cannot be calculated on the edges of the MHD simulation box where $B_x(x, y)$ and $B_y(x, y)$ are discontinued). $|J_z|$ is calculated from $4\pi J_z = \frac{\partial B_y}{\partial x} - \frac{\partial B_x}{\partial y}$, taking the absolute value. $|J_z|_{ss}$ is calculated with eq. (1), where "ss" represents authors of the method, Semel & Skumanich. In this work, the derivatives are replaced with the differences between neighboring pixels on the x-y plane:

$$\frac{\partial B_y}{\partial x} - \frac{\partial B_x}{\partial y} \approx \frac{B_y(x + \Delta x, y) - B_y(x - \Delta x, y)}{2\Delta x} - \frac{B_x(x, y + \Delta y) - B_x(x, y - \Delta y)}{2\Delta y}, \quad (4)$$

where Δx and Δy are the grid unit on the x- and y-axes, respectively. The approximation of derivatives to differences gives rise to numerical errors. These errors are introduced to both true $|J_z|$ and derived current densities $|J_z|_{ss}$; but they are squared in the $|J_z|_{ss}$ because the differences are carried out for B_x^2, B_y^2, B_xB_y between neighboring pixels in eq. (1). The smaller are the Δx and Δy, the better are the approximations.

Figure 2 shows maps of $\Delta J_z = |J_z| - |J_z|_{ss}$. These maps highlight pixels where large disagreements between $|J_z|$ and $|J_z|_{ss}$ occur. Figure 3 shows maps of $\Delta J_z/J_z$ representing the fractional errors in derived current density. Small values of $|\Delta J_z|$ over weak current densities are given equal erroneous impressions to those large values of $|\Delta J_z|$ over strong current densities.

Table 1 presents quantitative evaluations of eq. (1) when the current densities are calculated with models at the times $t = 30, 45, 56$. The analyses are conducted over pixels selected by two criteria: $|\Delta J_z| \geqslant 0.005$ (Case 1) and $|\Delta J_z/J_z| \geqslant 0.5$ (Case 2). The percentages of problematic pixels in either case are listed in columns 1st and 5th of Table 1. The average errors on $|J_z|_{ss}$ calculation are calculated by taking median values of $|\Delta J_z|$ over selected pixels for cases 1 and 2 (2nd and 6th columns, respectively). The medians of $[|J_z|, |J_z|_{ss}]$ are presented in the 3rd, 4th, and 7th, 8th columns, respectively, over respective sets of pixels defined by either $|\Delta J_z| \geqslant 0.005$ or $|\Delta J_z/J_z| \geqslant 0.5$. Figure 4 shows the correlation between $|J_z|$ (x-axis) and $|J_z|_{ss}$ (y-axis). All pixels are represented by a dot. Pixels where $|\Delta J_z| \geqslant 0.005$ are marked by "$\diamond$" symbols as well.

3 Discussion

Within entire simulation planes, we found that the average $|J_z|_{ss}$ and $|J_z|$ are very close to each other.

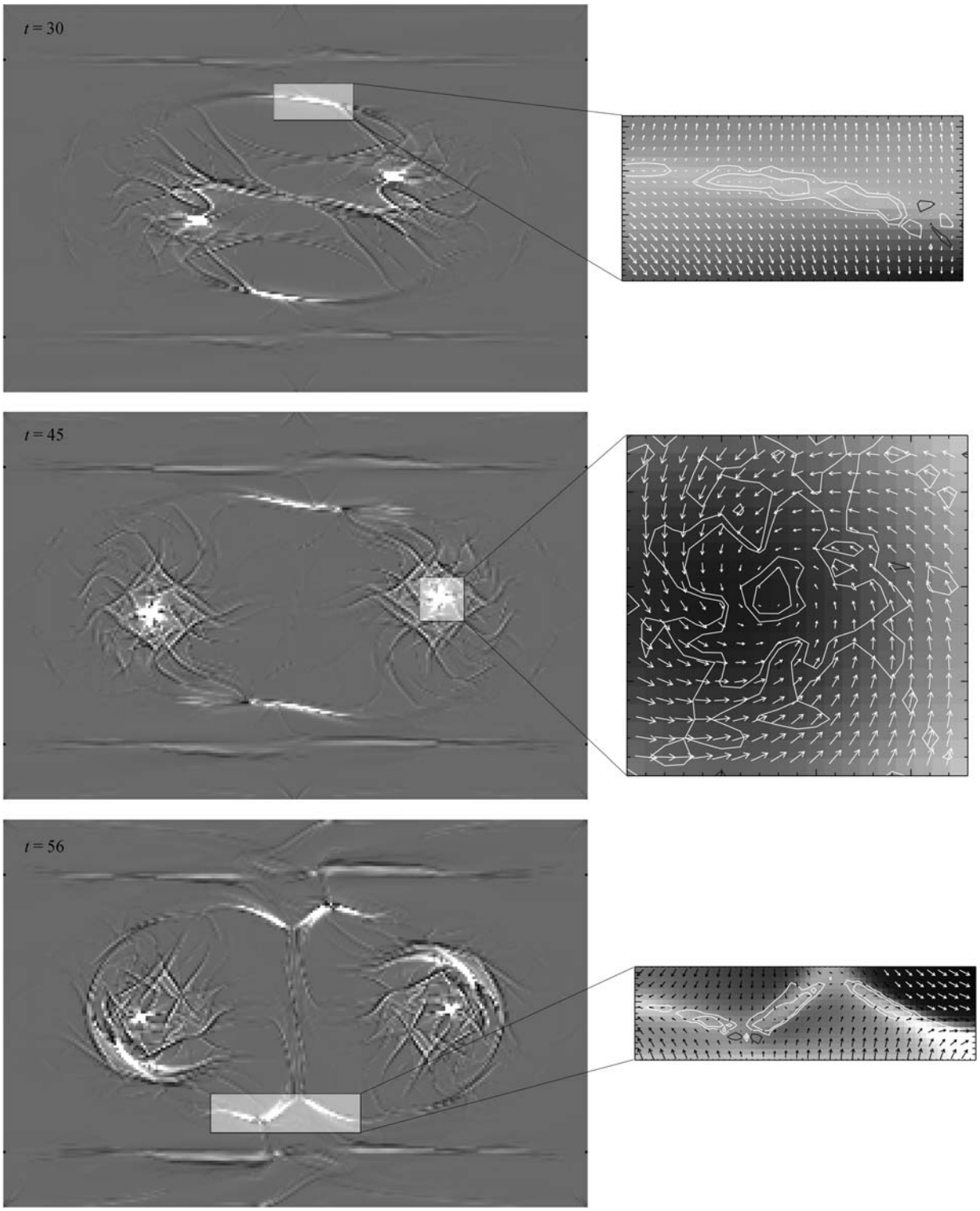

Figure 2 Demonstration of Type 1 error. Left: $\Delta J_z = |J_z| - |J_z|_{ss}$ at three times $T = 30, 45, 56$ from the top to the bottoms. The black- and white-most brightness represent [−0.005,0.005]. Small white translucent boxes highlight the area where $|J_z|$ and $|J_z|_{ss}$ disagree with large uncertainties. Right: Vector magnetic fields within corresponding highlighted translucent boxes, whose bars and the background images have the same meanings as those in Figure 1. The contours represent $\Delta J_z = |J_z| - |J_z|_{ss} = -0.1, -0.05, -0.005, -0.002, 0.002, 0.005, 0.05, 0.1$. White contours represent $\Delta J_z > 0$ and black contours represent $\Delta J_z < 0$.

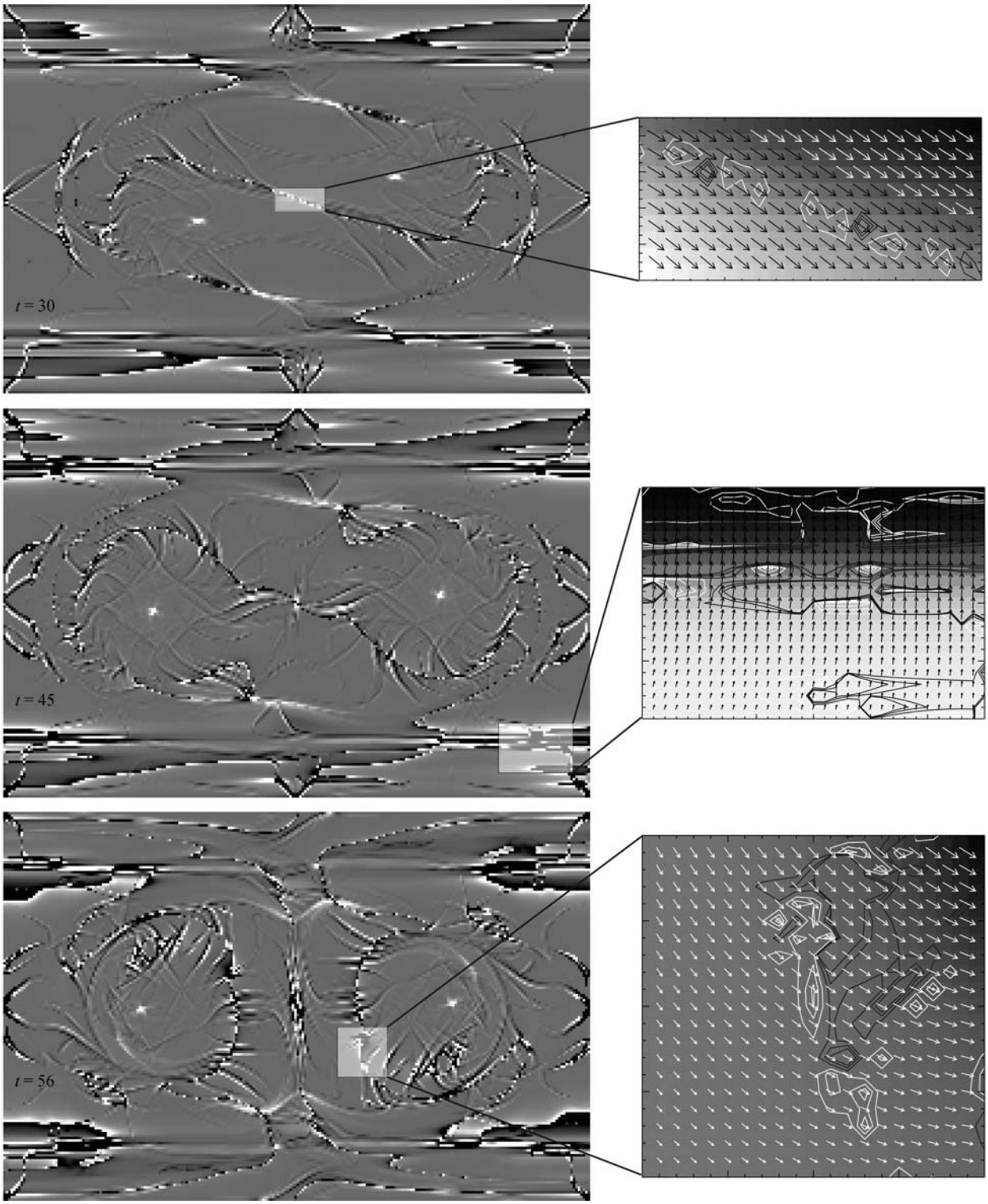

Figure 3 Demonstration of Type 2 error. Left: $\Delta J_z/J_z$ at three times $T = 30, 45, 56$ from the top to the bottoms; the black- and white-most brightness represent [−0.5,0.5]. Small white translucent boxes highlight the area where large ratios $\Delta J_z/J_z$ occur. Right: Vector magnetic fields within corresponding highlighted translucent boxes: background image is the vertical magnetic components; the short bars represent the horizontal magnetic fields. The contours represent $\Delta J_z = |J_z| - |J_z|_{ss} = -0.75, -0.5, -0.2, 0.2, 0.5, 0.75$. White contours represent $\Delta J_z/J_z > 0$ and black contours represent $\Delta J_z/Jz < 0$.

Table 1 Statistical analyses over pixels

	Case 1: Pixels ($\|\Delta J_z\| \geqslant 0.005$)				Case 2: Pixels ($\|\Delta J_z/J_z\| \geqslant 0.5$)			
		median				median		
Time	pixel %	$\|\Delta J_z\|$	$\|J_z\|$	$\|J_z\|_{ss}$	Pixel %	$\|\Delta J_z\|$	$\|J_z\|$	$\|J_z\|_{ss}$
30	0.308	8.97×10^{-3}	0.092	0.049	3.941	5.54×10^{-5}	5.09×10^{-5}	6.13×10^{-5}
45	0.425	8.35×10^{-3}	0.193	0.166	6.515	8.42×10^{-5}	5.70×10^{-5}	9.42×10^{-5}
56	0.675	7.97×10^{-3}	0.060	0.047	7.143	1.22×10^{-4}	8.05×10^{-5}	1.22×10^{-4}
Column	1st	2nd	3rd	4th	5th	6th	7th	8th

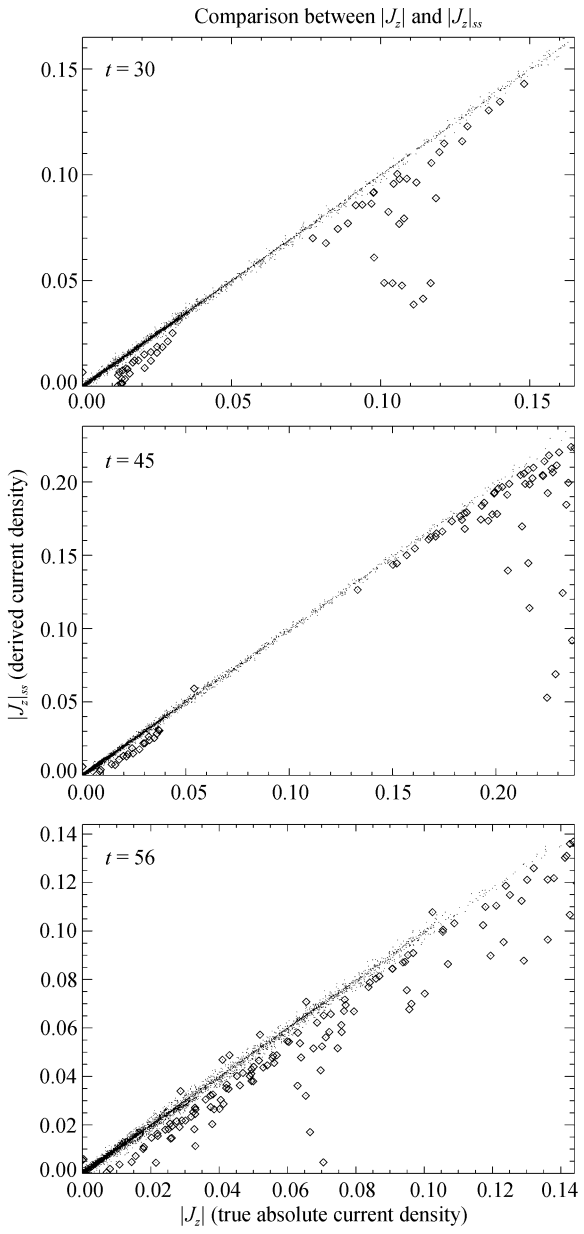

Figure 4 $|J_z|$ versus $|J_z|_{ss}$ at three times points, $t = 30, 45, 56$. The dots represent all pixels within the x-y plane. The "◇" symbols represent pixels having $|\Delta J_z| > 0.005$, most of them represent Type 1 errors.

The r.m.s. ($|J_z|$) are 0.02192, 0.0251 and 0.0211 for models at t=30, 45 and 56, respectively. In comparison, the r.m.s. ($|J_z|_{ss}$) are 0.0168, 0.0244, and 0.0207. They are slightly smaller than those $|J_z|$ by a factor typically $1.01 - 1.03$. On the other hand, large differences between $|J_z|$ and $|J_z|_{ss}$ occur on some special pixels which are demonstrated in Cases 1 and 2.

Numbers of pixels in Case 1 are only a few per thousand pixels (1st column in Table 1). Over these pixels, the median $|J_z|$ (3rd column) are stronger than average $|J_z|$ of the entire simulation planes by factors $12, 24$, and 7 suggesting strong current densities concentrate on these pixels. Examination of Table 1 and Figures 1 and 2 shows that the combination of vanishing horizontal field strength and dramatic changes in the magnetic azimuth results in large errors. Examples of problematic pixels are marked by yellow rectangles in Figure 2. On the right hand side, the rectangles are enlarged to demonstrate the horizontal magnetic field in all pixels. The vertical magnetic components are the background images, and the ΔJ_z are plotted in contours. This confirms what had been discussed by Semel & Skumanich[1] that the method fails on pixels where the magnetic field lines are discontinuous. We call errors originate from discontinuous field lines Type 1 error.

When the 3rd is compared with the 4th columns in Table 1, the Type 1 error results because $|J_z|_{ss}$ underestimates the true $|J_z|$ by factors $1.9, 1.2$, and 1.3. This is also evident in Figure 4 where the majority of "◇" symbols fall below the $|J_z| = |J_z|_{ss}$ line. This can be understood as a result of the "blind" calculation of $|J_z|_{ss}$. The dramatic change in the magnetic azimuth causes increasing magnitude in $|J_z|$, but eq. (1) assumes the most close

magnetic azimuths between neighboring pixels, resulting in smaller $|J_z|_{ss}$.

The numbers of pixels in Case 2 are a few percent of the total number of pixels (5th column in Table 1). Unlike magnetic fields on pixels in Case 1, the horizontal magnetic fields are neither vanishing nor experiencing dramatic changes in the azimuth on pixels in Case 2. The sample pixels are demonstrated on the right hand side of Figure 3, corresponding to the yellow rectangles on the $\Delta J_z/J_z$ maps. The median $|J_z|$ (7th column) are only a few hundredth of the average $|J_z|$, indicating that the vertical current densities are generally weak on these pixels. Finite differences are squared in the eq. (1) and are probably responsible for this kind of error. We call it Type 2 error.

The problematic pixels demonstrated in Case 2 are 10 times more numerous than those pixels demonstrated in Case 1 (1st and 5th columns). But the median differences between $|J_z|$ and $|J_z|_{ss}$ in Case 2 are more than 100 times as small as those in Case 1 (2nd and 6th columns). These mean that the dominant errors of the eq. (1) is Type 1 error. In addition, the median $|J_z|$ in Case 1 are much stronger than those median $|J_z|$ in Case 2 by factors 1807, 3385 and 745 (3rd and 7th columns). This means that Type 1 error often occurs over strong vertical current densities. Type 2 error only becomes prominent where current densities are weak. In real observations, Type 2 error can be omitted because it is 2 magnitudes smaller than that of the Type 1 error.

4 Summary

Equation (1), proposed by Semel & Skumanich[16], provide one more tool to estimate the vertical current density from vector magnetic field observations in the observing plane. Their method is free of the disambiguation of 180° in the transverse field directions, and therefore, removes an uncertainty from the J_z calculation. We apply the Semel & Skumanich formula to a MHD numerical simulation[20,21] to explore the limits of the method. We have identified two types of errors in the method. Dramatic changes in the magnetic azimuths with vanishing horizontal fields result in Type 1 error. The approximation of the derivatives to differences results in Type 2 error. A summary is given below.

1. Equation (1) accurately measures the vertical current density in a majority of pixels ($> 95\%$) in the observing plane.

2. Type 1 error results from the combination of vanishing horizontal fields and dramatic changes in the magnetic azimuth. The errors occur because of an inherent insufficiency in the absolute current density calculation proposed by Semel & Skumanich[16].

3. Type 2 error results in the approximations of derivatives to differences, which are squared in the Semel & Skumanich[16] calculations. Errors become prominent where current densities are weak.

4. Type 1 error is about 100 times as large as Type 2 error. In real observations, Type 2 error can be omitted.

5. When errors occur, the derived current density is smaller than the actual current density by factors typically $1.2 - 1.9$.

6. The number of unreliable pixels increases with the increasing number of twists in the magnetic flux tube system above the boundary.

JL would like to thank David Jewitt for his comments on the manuscript, and patient editions on the English writing. JL would also like to thank Dr. Yu Lu for his comments which greatly improved the paper. University Research Council (URC), University of Hawaii, supported JL's travel to attend the Solar Eclipse Conference in Jiuquan, China, July–August 2008.

1 Deloach A C, Hagyard M J, Rabin D, et al. Photospheric electric current and transition region brightness within an active region. Sol Phys, 1984, 91: 235–242

2 Lin Y, Gaizauskas V. Coincidence between Halpha flare kernels and peaks of observed longitudinal electric current densities. Sol Phys, 1987, 109: 81–90

3 Hagyard M J. Observed nonpotential magnetic fields and the inferred flow of electric currents at a location of repeated flaring. Sol Phys, 1988, 115: 107–124

4 Canfield R C, Hudson H S, Leka K D, et al. The X flare of 1991 November 15 - Coordinated Mees/Yohkoh observations. Publ Astron Soc Jpn, 1992, 44: L111–115

5 Leka K D, Canfield R C, McClymont A N, et al. The morphology of flare phenomena, magnetic fields, and electric currents

in active regions. II - NOAA active region 5747 (1989 October). Astrophys J, 1993, 411: 370–377
6 de La Beaujardiere J -F, Canfield R C, Leka K D. The morphology of flare phenomena, magnetic fields, and electric currents in active regions. III - NOAA active region 6233 (1990 August). Astrophys J, 1993, 411: 378–382
7 Zhang H, Wang T. Vertical current and a 3B/X12 flare in a highly sheared active region (NOAA 6659) on June 9, 1991. Sol Phys, 1994, 151: 129–136
8 Wu S T, Weng F S, Wang H M, et al. Magnetic structures and energy of 1989 March flares. Adv Space Res, 1993, 13: 127–130
9 van Driel-Gesztelyi L, Hofmann A, Demoulin P, et al. Relationship between electric currents, photospheric motions, chromospheric activity, and magnetic field topology. Sol Phys, 1994, 149: 309–330
10 Metcalf T R, Canfield R C, Hudson H S, et al. Electric currents and coronal heating in NOAA active region 6952. Astrophys J, 1994, 428: 860–866
11 Gary G A, Demoulin P. Reduction, analysis, and properties of electric current systems in solar active regions. Astrophys J, 1995, 445: 982–998
12 Li J, Metcalf T R, Canfield R C, et al. What is the spatial relationship between hard X-ray footpoints and vertical electric currents in solar flares? Astrophys J, 1997, 482: 490-497
13 Burnette A B, Canfield R C, Pevtsov A A. Photospheric and coronal currents in solar active regions. Astrophys J, 2004, 606: 565–570
14 Gary A, Moore R L. Eruption of a multiple-turn helical magnetic flux tube in a large flare: Evidence for external and internal reconnection that fits the breakout model of solar magnetic eruptions. Astrophys J, 2004, 611: 545–556
15 Gao Y, Xu H, Zhang H. Probing the method of correcting Faraday rotation in vector magnetograms. Adv Space Res, 2008, 42: 888–894
16 Semel M, Skumanich A. An ambiguity-free determination of J_Z in solar active regions. Astron Astrophys, 1998, 331: 383–383
17 Li J, van Ballegooijen A, Mickey D. Vector magnetic fields and electric currents from the imaging vector magnetograph. Astrophys J, 2009, 692: 1543–1560
18 Li J, Mickey D L, LaBonte B J. The X3 Flare of 2002 July 15. Astrophys J, 2005, 620: 1092–1100
19 Cowling T G. The electrical conductivity of an ionized gas in a magnetic field, with applications to the solar atmosphere and the ionosphere. R Soc Lond Proc Ser A, 1945, 183: 453–479
20 Fan Y, Gibson S E. The emergence of a twisted magnetic flux tube into a preexisting coronal arcade. Astrophys J Lett, 2003, 589: L105–108
21 Fan Y, Gibson S E. Numerical simulations of three-dimensional coronal magnetic fields resulting from the emergence of twisted magnetic flux tubes. Astrophys J, 2004, 609: 1123–1133